

# Jasmine: Harnessing Diffusion Prior for Self-Supervised Depth Estimation

Jiyuan Wang<sup>1</sup>, Chunyu Lin<sup>1†</sup>, Cheng Guan<sup>1</sup>, Lang Nie<sup>1</sup>  
 Jing He<sup>2</sup>, Haodong Li<sup>2</sup>, Kang Liao<sup>3</sup>, Yao Zhao<sup>1</sup>  
<sup>1</sup>BJTU, <sup>2</sup>HKUST, <sup>3</sup>NTU, <sup>†</sup>Corresponding author

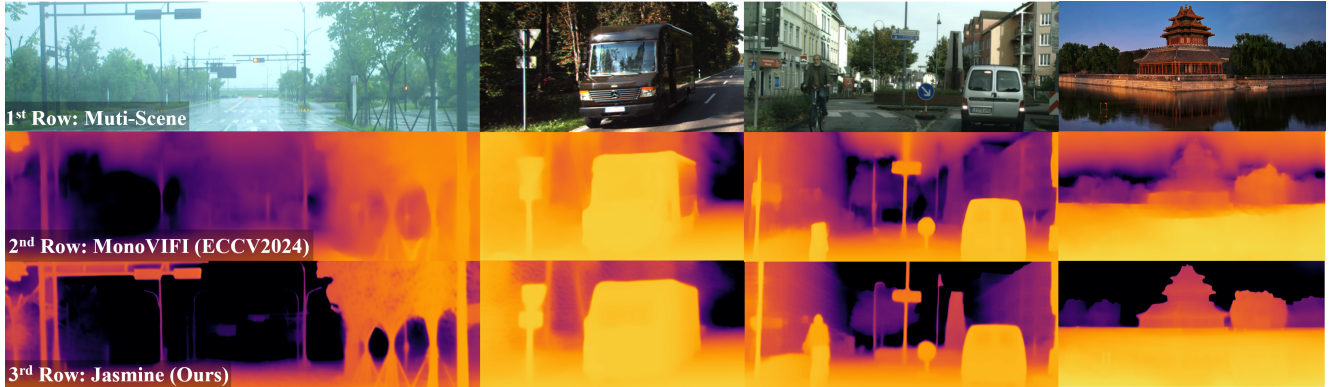


Figure 1. **Without any high-precision depth supervision**, Jasmine achieves remarkably detailed and accurate depth estimation results through zero-shot generalization across diverse scenarios.

## Abstract

In this paper, we propose **Jasmine**, the first Stable Diffusion (SD)-based self-supervised framework for monocular depth estimation, which effectively harnesses SD’s visual priors to enhance the sharpness and generalization of unsupervised prediction. Previous SD-based methods are all supervised since adapting diffusion models for dense prediction requires high-precision supervision. In contrast, self-supervised reprojection suffers from inherent challenges (e.g., occlusions, texture-less regions, illumination variance), and the predictions exhibit blurs and artifacts that severely compromise SD’s latent priors. To resolve this, we construct a novel surrogate task of hybrid image reconstruction. Without any additional supervision, it preserves the detail priors of SD models by reconstructing the images themselves while preventing depth estimation from degradation. Furthermore, to address the inherent misalignment between SD’s scale and shift invariant estimation and self-supervised scale-invariant depth estimation, we build the Scale-Shift GRU. It not only bridges this distribution gap but also isolates the fine-grained texture of SD output against the interference of reprojection loss. Extensive experiments demonstrate that Jasmine achieves SoTA performance on the KITTI benchmark and exhibits superior zero-shot generalization across multiple datasets.

## 1. Introduction

Estimating depth from monocular images is a fundamental problem in computer vision, which plays an essential role in various downstream applications such as 3D/4D reconstruction[48], autonomous driving[10], etc. Compared with supervised methods[21, 32], self-supervised monocular depth estimation (SSMDE) mines 3D information solely from video sequences, significantly reducing reliance on expensive ground-truth depth annotations. These methods derive supervision from geometric constraints (e.g., scene depth consistency) through cross-frame reprojection loss, and the ubiquitous video data further suggests an unlimited working potential. However, view reconstruction-based losses suffer from occlusions, texture-less regions, and illumination changes[56], which severely restrict the model’s capacity to recover fine-grained details and may cause pathological overfitting to specific datasets.

Recent studies[24] demonstrated that SD possesses powerful visual priors to elevate depth prediction sharpness and generalization, which offers promising potential to address the above limitations. In addition, E2E FT[32] and Lotus[21] further reveal that single-step denoising can achieve better accuracy, which is particularly critical for self-supervised paradigms. It not only accelerates the inference denoising process but also significantly reduces the training costs in self-reprojection supervision, thereby creating opportunities to integrate SD into the SSMDE frame-

work.

However, fine-tuning diffusion models for dense prediction requires high-precision supervision to preserve their inherent priors[24]. Supervised methods typically employ synthetic RGB-D datasets, where clean depth annotations align with the high-quality SD’s training data, thereby keeping its latent space intact. In contrast, directly applying self-supervision introduces a critical challenge: reprojection losses or pre-trained depth pseudo-labels propagate perturbed gradients caused by artifacts and blurs into SD’s latent space, rapidly corrupting its priors during early training stages. Namely, high-precision “supervision” must exist at the beginning to protect SD’s latent space. Such supervision seems impossible in self-supervised learning, but we ingeniously find a handy and valuable alternative: the RGB image. In fact, the image inherently contains complete visual details, avoids external depth dependencies in self-supervision, and aligns perfectly with SD’s original objective of image generation. Therefore, we construct a surrogate task of hybrid image reconstruction through a task switcher, where the same SD model alternately reconstructs synthesized/real images and predicts depth maps within each training batch. This strategy repurposes self-supervised reprojection loss to tolerate color variations while maintaining structural consistency, intentionally decoupling color fidelity from depth accuracy, and finally preserving SD priors successfully.

Another challenge is the output range of SD’s VAE that is inherently bounded within a fixed range, *i.e.*,  $[-1, 1]$ . Existing methods typically normalize GT depth maps to this range in the training procedure. During inference, these supervised approaches perform least-squares alignment to recover absolute scale and shift, yielding scale- and shift-invariant (SSI) depth predictions. However, self-supervised frameworks rely on coupled depth-pose optimization, which theoretically requires shift invariance to be strictly zero for stable convergence, ultimately producing scale-invariant (SI) depth predictions. To bridge this inherent distribution gap, we propose a novel transform module termed Scale-Shift GRU (SSG). It not only iteratively aligns SSI depth to SI depth by refining scale-shift parameters but also acts as a gradient filter, which suppresses anomalous gradients caused by artifact-contaminated in self-supervised training, thereby preserving the fine-grained texture details of SD’s output while enforcing geometric consistency.

Extensive experiments show that our proposed method, Jasmine, achieves the SoTA performance among all SS-MDEs on the competitive KITTI dataset, shows remarkable zero-shot generalization across multiple datasets (even surpassing models trained with augmented data), and demonstrates unprecedented detail preservation. To sum up, the main contributions are summarized as follows:

- We **first** introduce SD into a self-supervised depth estima-

tion framework. Our methods eliminate the dependency on high-precision depth supervision while retaining SD’s inherent advantages in detail sharpness and cross-domain generalization.

- We proposed a surrogate task of HIR that anchors SD’s priors via self-supervised gradient sharing to avoid SD’s latent-space corruption caused by reprojection artifacts.
- We proposed Scale-Shift GRU (SSG) to dynamically align depth scales while filtering noisy gradients to solve SSI versus SI distribution mismatch problems in self-supervised depth estimation.

## 2. Relative Work

**Self-supervised Depth Estimation** Due to the high costs of GT-depth collection from LiDARs and other sensors, self-supervised depth estimation (SSDE) has gained significant research attention. SSDE can be broadly categorized into stereo-based (learning depth from synchronized image pairs)[2, 3, 12, 14, 45] and monocular-based methods (using sequential video frames)[19, 20, 28, 30, 31, 33, 36, 54, 56, 58, 60]. Compared to the stereo ones, monocular approaches eliminate the need for synchronized binocular cameras and calibration, though they face challenges with dynamic objects and pose estimation inaccuracy. Additionally, when focusing on monocular video training, existing methods further diverge into single-frame and multi-frame approaches. Single-frame models neglect temporal information during inference, while multi-frame methods[1, 9, 17, 46, 47] leverage consecutive frames to construct cost volumes and even support iterative refinement at test time, yielding improved accuracy. However, the practical deployment of these methods remains constrained by the availability of multiple frames. Recently, the progress of DepthAnything v1/v2[50, 51] has revealed that, by training on large-scale image depth pairs, we can obtain an accurate single image depth prediction model with strong generalization. However, we argue that such datasets still remain a small fraction of the ubiquitous video data available. This observation motivates our exploration of the most challenging configuration: training exclusively on video sequences while maintaining single-frame inference capability, thereby laying the groundwork for developing genuinely versatile “DepthAnything” models.

**Diffusion for Depth Perception** As the diffusion paradigm showcases its talents in generative tasks[22, 27, 42, 52], DDP[23] first reformulates depth perception as a depth map denoising task and leads to giant progress. Followers like DDVM[39], MonoDiffusion[41], and D4RD[44] (the latter two are self-supervised methods) all demonstrate the advantages of this paradigm in various MDE sub-tasks. Subsequently, the most renowned diffusion model, Stable Diffusion[38], has demonstrated significant

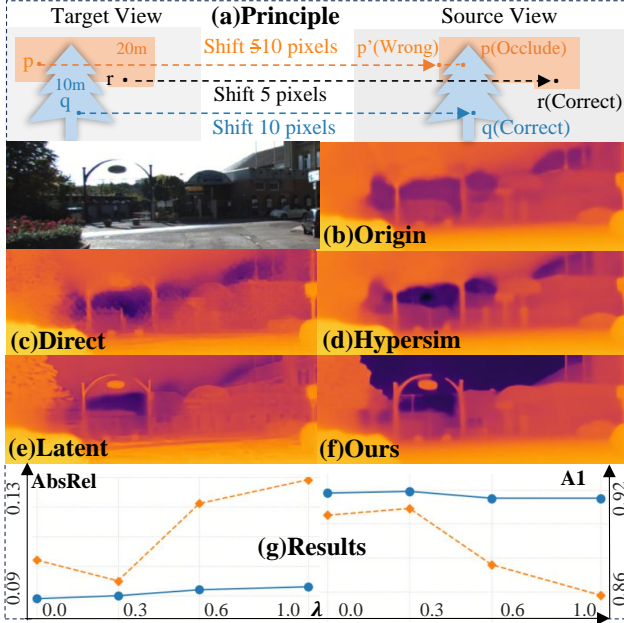


Figure 2. **The attempts to preserve the SD prior.** The meanings of (a)-(f) are detailed in Sec. 3.2. Notably, while (e) demonstrates superior visual quality, it erroneously interprets surface textures (e.g., house windows) as depth edges. (g) shows the performance variations under different  $\lambda$  settings for **Ph supervision** (Eq. 7) and **latent supervision** (Eq. 6). The complete metrics and their definitions are provided in the supplementary material.

potential for depth perception tasks. VPD[57], TAPD[25], and Prior-Diffusion[53] use Stable Diffusion as a multi-modal feature extractor, leveraging textual modality information to improve depth estimation accuracy. Concurrently, Marigold[24] and GeoWizard[11] enhanced model generalization and detail preservation by fine-tuning Stable Diffusion, capitalizing on its prior training with large-scale, high-quality datasets. Afterward, E2E FT[32] and Lotus[21] further accelerated inference by optimizing the noise scheduling process. In this work, our Jasmine continues these works and extends SD to the field of self-supervision.

### 3. Methods

In this section, we will introduce the foundational knowledge of the SSMDE and SD-based MDE (Sec. 3.1), the surrogate task of hybrid image reconstruction (Sec. 3.2), the scale-shift adaptation with GRU (Sec. 3.3) and the SD fine-tune protocol specified for self-supervision (Sec. 3.4). An overview of the whole framework is shown in Fig. 3.

#### 3.1. Preliminaries

**Self-Supervised Monocular Depth Estimation** makes use of the adjacent frames  $\mathbf{I}_{t'}$  to supervise the output depth with geometric constraints. Given the current frame  $\mathbf{I}_t$ , the MDE model as  $\mathcal{F} : \mathbf{I}_t \rightarrow D \in \mathbb{R}^{W \times H}$ , we can synthesize a warped

current frame  $\mathbf{I}_{t' \rightarrow t}$  with:

$$\mathbf{I}_{t' \rightarrow t} = \mathbf{I}_{t'} \langle \text{proj}(D, \mathcal{T}_{t \rightarrow t'}, K) \rangle, t' \in (t-1, t+1), \quad (1)$$

where  $\mathcal{T}_{t \rightarrow t'}$  denotes the relative camera poses obtained from the pose network,  $K$  denotes the camera intrinsics, and  $\langle \cdot \rangle$  denotes the grid sample process. Then, we can compute the photometric reconstruction loss between  $\mathbf{I}_t$  and  $\mathbf{I}_{t' \rightarrow t}$  to constrain the depth:

$$L_{ph} = \eta_{p1} \frac{1 - \text{SSIM}(\mathbf{I}_t, \mathbf{I}_{t' \rightarrow t})}{2} + \eta_{p2} \|\mathbf{I}_t - \mathbf{I}_{t' \rightarrow t}\|. \quad (2)$$

**Stable Diffusion-based Monocular Depth Estimation** reformulates depth prediction as an image-conditioned annotation generation task. Typically, given the image  $\mathbf{I}$  and processed GT depth  $\mathbf{y}$ , SD first encodes them to the low-dimension latent space through a VAE encoder  $\varepsilon$ , as  $\mathbf{z}^I, \mathbf{z}^y = \varepsilon(\mathbf{I}, \mathbf{y})$ . Afterward, gaussian noise is gradually added at levels  $\tau \in [1, T]$  into  $\mathbf{z}^y$  to obtain the noisy sample, with  $\mathbf{z}_\tau^y = \sqrt{\bar{\alpha}_\tau} \mathbf{z}^y + \sqrt{1 - \bar{\alpha}_\tau} \epsilon$ , then the model learns to iteratively reverse it by removing the predicted noise:

$$\hat{\epsilon} = f_\theta^\epsilon(\mathbf{z}_{\tau-1}^y | \mathbf{z}_\tau^y, \mathbf{z}^I), \quad (3)$$

and finally decodes the depth prediction with  $D = \mathcal{D}(\mathbf{z}_0^y)$ . Here  $\epsilon \sim \mathcal{N}(0, I)$ ,  $f_\theta^\epsilon$  is the  $\epsilon$ -prediction UNet,  $\bar{\alpha}_t := \prod_{s=1}^t (1 - \beta_s)$ , and  $\{\beta_1, \beta_2, \dots, \beta_T\}$  is the noise schedule with  $T$  steps.

Equation 1 demonstrates that the self-supervised approach needs the depth prediction  $D$  for image warping. However, obtaining  $\mathbf{z}_0^y$  requires iterative computation of Eq. 3, a process that becomes computationally infeasible considering the enormous size of SD models. Luckily, Lotus and E2E FT[21, 32] demonstrate that we can obtain comparable results with single-step denoising and directly predict depth,

$$D = \mathcal{D}(f_\theta^z(\mathbf{z}_\tau^y, \mathbf{z}^I)), \tau = T, \quad (4)$$

which makes it possible to train SD with self-supervision.

#### 3.2. Surrogate Task: Image Reconstruction

**Motivation.** The photometric reconstruction losses (Eq. 2) inevitably introduce the supervision with noise and artifacts due to occlusions, texture-less regions, and photometric inconsistencies. As shown in Fig. 2 (a), consider a scenario that  $\mathcal{T}_{t \rightarrow t'}$  represents a pure horizontal translation. The point  $p$ —which should ideally have 5 pixels of disparity (reciprocal of depth)—becomes occluded. It must instead displace 10 pixels to compensate for incorrect pixel matches, resulting in erroneous depth alignment with point  $q$ . This phenomenon propagates to neighboring points, collectively eroding structural details (e.g., the tree’s edge) while generating imprecise supervisory signals that rapidly degrade SD’s fine-grained prior knowledge.

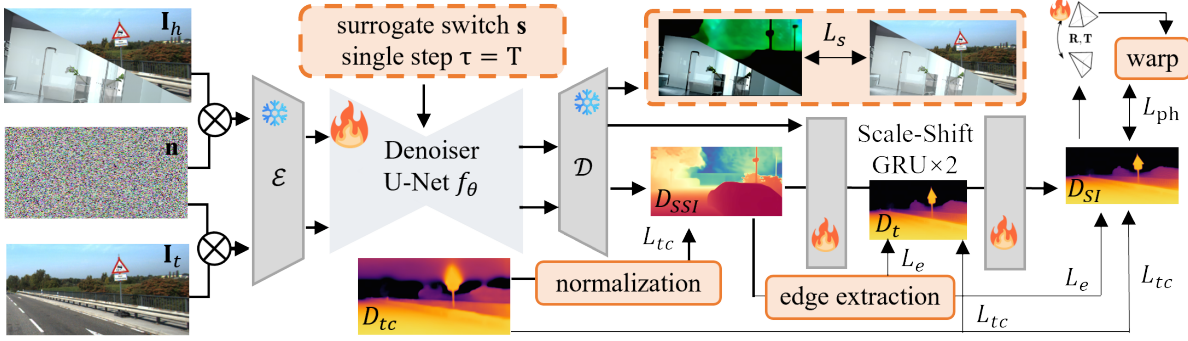


Figure 3. **Finetuning Protocol of Jasmine.** The whole pipeline only contains 3 trainable modules: U-Net, Posenet, and Scale-Shift GRU (SSG). The other components are all frozen, including the encoder  $\varepsilon$  and the decoder  $\mathcal{D}$ . In the beginning, the training image  $\mathbf{I}_t$  and the hybrid image  $\mathbf{I}_h$  are both concatenated with zero-noise  $\mathbf{n}$ [32] and fed into the  $\varepsilon$ . Next, the U-Net performs single-step denoising guided by the task switcher  $s$ , and subsequently decodes the depth prediction  $D_{SSI}$  and the reconstructed image  $\mathbf{I}$  with the  $\mathcal{D}$  (Eq. 5). Afterward, the SSI-depth prediction is processed by the SSG for distribution refinement, yielding the final depth estimate  $D_{SI}$ . Supervision signals (right part) are detailed in Sec. 3.4.

To preserve these details, we notice that both SSMDE and SD inherently rely on image consistency: SSMDE uses photometric constraints (Eq. 2), while SD’s training directly minimizes image generation errors. Inspired by this, we propose a surrogate task: image reconstruction. Concretely, following [11], we also design a switcher  $s \in \{s_x, s_y\}$  to alternate the Unet  $f_\theta^z$  between the main and surrogate tasks:

$$[D, \mathbf{I}] = \mathcal{D}(f_\theta^z([s_x, s_y], \mathbf{z}_t^y, \mathbf{z}^{\mathbf{I}})). \quad (5)$$

Therefore, we follow the SD paradigm and initially formulate the surrogate loss as:

$$L_s = \|\mathbf{z}^{\mathbf{I}} - f_\theta^z(\mathbf{z}^{\mathbf{I}}, t, s_y)\|^2. \quad (6)$$

**Hybrid Images and Reconstruction Loss.** We show that it is possible to preserve the SD priors by introducing a compact surrogate task. However, our experiments reveal that naively applying Eq. 6 for SSMDE optimization yields sub-optimal results (Fig. 2(c)). Through empirical investigation, we identify three critical insights: **1)** Reconstruction of inferior quality images (*e.g.*, KITTI) introduces block artifacts (Fig. 2(c)). We attribute this to the latent space operating at  $\frac{1}{8}$  resolution: When inputs align with the pre-trained  $\varepsilon$  and  $\mathcal{D}$ , smooth supervision is achieved. Conversely, each latent pixel supervision manifests as  $8 \times 8$  block artifacts in prediction. **2)** Introducing high-quality synthesized images (maintaining self-supervision compliance) offers a potential solution, but exclusive reconstruction of synthetic data causes task decoupling and preserves depth prediction blurriness (Fig. 2 (d)). **3)** Blending these images with a ratio  $\lambda$  allows synthesized images to anchor the model to latent priors while real-world data enforces geometric structure alignment, is a possible solution. But this strategy shows notable sensitivity to  $\lambda$  (Fig. 2 (g), (e) is a failure scene).

To address this VAE-Image mismatch, we proposed to replace Eq. 6 with the photometric loss  $L_{ph}$  (Eq. 2)

in the image domain. Compared to Eq. 6,  $L_{ph}$  emphasizes structural consistency rather than color fidelity, which aligns better with depth estimation objectives. As shown in Fig. 2(f, g), this supervision not only makes hybrid image reconstruction robust to  $\lambda$  but also significantly improves the estimation quality. Therefore, we take the Hypersim dataset(4.2.1), a photorealistic synthetic dataset specifically designed for geometric learning, as the auxiliary image and update Eq. 6 with

$$\mathbf{I}_h = R_c(\mathbf{I}_K, \mathbf{I}_H, \lambda), L_s = L_{ph}(\mathbf{I}_h, \mathcal{D}(f_\theta^z(\mathbf{z}^{\mathbf{I}}, t, s_y))), \quad (7)$$

where  $R_c$  denotes random choice and  $\mathbf{I}_K/\mathbf{I}_H$  is KITTI/Hypersim images.

**Analysis of Auxiliary Images** The specific synthetic data usage may raise concerns about applicability boundaries. To clarify, we conduct additional experiments and present three insights about the relationship between auxiliary data and performance: (1) Synthetic images are not essential, our surrogate task maintains efficacy with real-world imagery. (2) The dataset scale proves non-critical, as competitive performance emerges with samples under 1k. (3) Domain divergence between auxiliary and primary datasets enhances results and is even more important than image quality. Please refer to Sec. 4.3 for detailed experimental support.

This analysis reveals HIR is a highly promising training paradigm. It not only imposes no inherent limitations on any dense prediction tasks but also challenges the notion that fine-tuning SD requires high-quality annotation. Even with legacy datasets like KITTI, we can still leverage readily available images to effectively utilize SD priors and enhance depth estimation sharpness.

### 3.3. Scale-Shift GRU

**The misalignment of SSI-SI depth.** SSMDE predicts Scale-Invariant Depth  $D_{SI}$ . Denoting  $\mathcal{T}_{t \rightarrow t'}$  as  $[\mathbf{R}|\mathbf{T}]$ , we

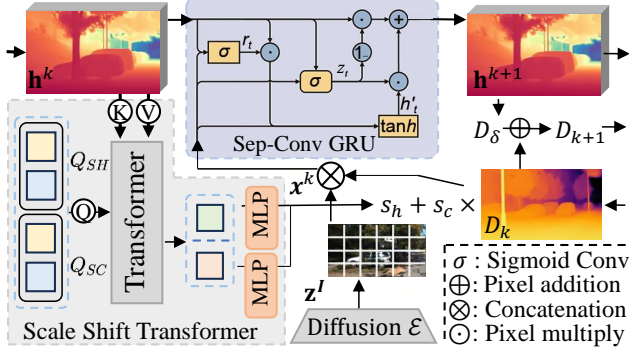


Figure 4. **Model Structure of Scale Shift GRU.** The implementation details are comprehensively described in Sec. 3.3.

can prove it by further expanding the *proj* process in Eq. 1 with:

$$\zeta' D' = K(\mathbf{R}K^{-1}\zeta D + \mathbf{T}), \quad (8)$$

where  $\zeta, \zeta'$  denote homogeneous coordinates and  $D, D'$  represent depths in  $\mathbf{I}_t$  and  $\mathbf{I}_{t'}$ , respectively. Afterward, the coordinate  $\zeta'[u, v]$  in  $\mathbf{I}_{t'}$  maps to  $[u, v]$  in  $\mathbf{I}_{t \rightarrow t'}$  and we can grid sample every pixel to get  $\mathbf{I}_{t' \rightarrow t}$ . However, this mapping is not unique. We can scale both sides of the equation with  $s_c$ :

$$\zeta' s_c D' = K(\mathbf{R}K^{-1}\zeta s_c D + s_c \mathbf{T}), \quad (9)$$

where both  $\mathbf{T}$  and  $s_c \mathbf{T}$  represent valid relative poses. But if we further introduce a shift  $s_h$ , we can derive the formula to obtain:

$$K^{-1}\zeta' g_1(D') = \mathbf{R}K^{-1}\zeta s_h + g_2(\mathbf{T}), \quad (10)$$

where  $g_1(\cdot)$  and  $g_2(\cdot)$  are affine invariant transformations. This means that the affine depth of any scene can appear as a plane from a certain perspective (the depth of the plane is  $s_h$ ), which is undoubtedly impossible. More detailed derivations are provided in the supplementary material Sec. A.

SD-based MDE predicts Scale-Shift-Invariant Depth  $D_{SSI}$ . The processed GT depth  $\mathbf{y}$  mentioned in Sec. 3.1 satisfy the VAE's inherently boundary  $[-1, 1]$ , typically obtained by:

$$\mathbf{y} = \left( \frac{D_{GT} - D_{GT,2}}{D_{GT,98} - D_{GT,2}} - 0.5 \right) \times 2, \quad (11)$$

where  $D_{GT,i}$  corresponds to the  $i\%$  percentiles of individual depth maps. Obviously,  $\mathbf{y}$  differs from  $D_{GT}$  by an absolute scale and shift, which can be recovered by the least squares alignment in evaluation.

This inherent distribution gap between SSI and SI depth creates barriers for SD integration, and the SSG is specifically designed to fix it.

**The Design of SSG.** Similar to recovering absolute depths, transforming depth distribution requires profound scene understanding, and the scale ( $s_c$ ) and shift ( $s_h$ ) are tight couplings. So as shown in Fig. 4, the core component Scale-Shift Transformer (SST) employs learnable scale/shift queries that interact with SD's hidden states (keys/values) via cross-attention. The output vector is split and processed by MLPs to predict  $s_c$  and  $s_h$ . To enhance spatial awareness, image features  $\mathbf{z}^I$  are concatenated with depth maps as current input  $\mathbf{x}^k$ . The hidden state  $\mathbf{h}^k$  evolves through reset  $\mathbf{r}^{k+1}$  and update  $\mathbf{z}^{k+1}$  gates:

$$\begin{aligned} \mathbf{z}^{k+1} &= \sigma([\mathbf{h}^k, \mathbf{x}^k], W_z), \mathbf{r}^{k+1} = \sigma([\mathbf{h}^k, \mathbf{x}^k], W_r), \\ \hat{\mathbf{h}}^{k+1} &= \tanh(\text{Conv}([\mathbf{r}^{k+1} \odot \mathbf{h}^k, \mathbf{x}^k], W_h)), \\ \mathbf{h}^{k+1} &= (1 - \mathbf{z}^{k+1}) \odot \mathbf{h}^k + \mathbf{z}^{k+1} \odot \hat{\mathbf{h}}^{k+1}, \end{aligned} \quad (12)$$

where  $k$  denotes iteration steps, and  $W_z, W_r, W_h$  stands for learnable parameters. The refined hidden state  $\mathbf{h}^{k+1}$  predicts depth adjustment  $D_\delta$  to update  $D_k$ , yielding  $D_{k+1}$  for subsequent iterations. To balance computational efficiency and GRU's iterative benefits, we employ two GRU iterations: starting from initial depth  $D_0$  ( $D_{SSI}$ ) to sequentially produce  $D_1$  and  $D_2$  ( $D_{SI}$ ).

GRU is preferred over other architectures due to its reset gate mechanism. This enables the fine-grained  $D_{SSI}$  to filter out erroneous supervision signals from reprojection losses. Particularly, in Eq. 12, the reset gate  $\mathbf{r}^{k+1}$  identifies regions requiring correction based on current inputs  $(\mathbf{h}^k, \mathbf{x}^k)$ , which are then element-wise multiplied with  $\mathbf{h}^k$  to compute  $\hat{\mathbf{h}}^{k+1}$ . This operation prevents the back-propagation of erroneous gradients to the former step during training. Overall, the SSG not only iteratively aligns SSI depth to SI depth by refining scale-shift parameters but also acts as a gradient filter, which suppresses anomalous gradients caused by artifacts, thereby preserving the fine-grained texture details of SD's output while enforcing geometric consistency.

### 3.4. Steady SD Finetune with Self-Supervision

In the experiment, we observed that the training process was significantly unstable, mainly due to the SD's enormous size, joint training across modules, and indirect self-supervisory mechanisms. To enhance the convergence reliability and reproducibility, we first introduced a pre-trained self-supervised teacher model (e.g., MonoViT) to estimate  $D_{tc}$  as pseudo labels.  $D_{tc}$  provides direct supervision but has a performance upper bound, which can stabilize model training in the early stages while gradually decreasing loss weights throughout the training process:

$$\begin{aligned} L_{tc} &= (L_B(\text{norm}(D_{tc}), D_{SSI}) + L_B(D_{tc}, D_1) \cdot \eta_{t1} \\ &\quad + L_B(\text{filter}(D_{tc}), D_{SI}) \cdot \eta_{t2}) / \eta_{\text{step}}, \end{aligned} \quad (13)$$

where  $L_B$  is the Berhu Loss, “norm” is the [-1,1] normalization, and “filter” are adaptive strategies to avoid performance bottlenecks, as detailed in the supplementary materials Sec. B.

Furthermore, we implement a module-wise freezing training strategy, which involves 3 key phases: In the beginning, we enable gradient updates for all network components. Subsequently, we freeze the SSG and Posenet modules to decouple depth-pose optimization while maintaining fixed parameters. After achieving convergence to a suboptimal solution, we reintroduce gradient updates to these modules for final optimization. Through extensive experimentation, we demonstrate this module-wise freezing training proves particularly crucial for steady training in complex, multi-module self-supervised systems.

Finally, the total training loss of the Jasmine model is:

$$L = L_s + L_{ph} + L_{tc} + L_a \cdot \eta_a, \quad (14)$$

where  $L_s$  refer to Eq.7,  $L_{ph}$  refer to Eq. 2,  $L_{tc}$  refer to Eq. 13, and  $L_a$  is some auxiliary adjustment losses (e.g. gds loss[33], edge loss, sky loss) with a tiny weight, and they will be detailed in supplementary material Sec. B.

## 4. Experiment

### 4.1. Implement Details

We implement the proposed Jasmine using Accelerate[16] and Pytorch[34] with Stable Diffusion v2[38] as the backbone. Following the pipeline in Fig. 3, we disable text conditioning while maintaining most hyperparameter consistency with E2E FT[32]. The loss weights specified in Sec. 3 are empirically configured as:

$$\eta_a = 8 \times 10^{-3}, \eta_{t1} = 0.6, \eta_{t2} = 0.9, \eta_{p1} = 0.85, \\ \eta_{p2} = 0.15, \eta_{step} = \max(1, 30 \cdot (\text{step}_{now} / \text{step}_{max})).$$

Training employs the AdamW optimizer[29] with a base learning rate of  $3 \times 10^{-5}$ . As outlined in Sec. 3.4, the first training phase involved 15k steps, while the second and third phases automatically transitioned, sharing an additional 10k steps for a total of 25k training steps. All experiments are conducted on 8 NVIDIA A800 GPUs with a total batch size of 32, requiring around 1 day. Following [15], we also employed standard data augmentation techniques (horizontal flips, random brightness, contrast, saturation, and hue jitter).

### 4.2. Evaluation

#### 4.2.1. Datasets

Unless specified, all datasets are finally resized to  $1024 \times 320$  resolution for training.

**Training Datasets.** KITTI[13]: Following the previous work[15], we mainly conduct our experiments on the

widely used KITTI dataset. We employ Zhou’s split[59] containing 39,810 training and 4,424 validation samples after removing static frames. The evaluation uses 697 Eigen raw test images with metrics from [15], applying 80m ground truth clipping and Eigen crop preprocessing[8]. Hypersim[37]: This photorealistic synthetic dataset (461 indoor scenes) contributes approximately 28k samples from its official training split for hybrid image reconstruction. Each iteration uses random crops from the original  $1024 \times 768$  to  $1024 \times 320$  resolution.

**Zero-shot Evaluation Datasets** DrivingStereo[49]: Contains 500 images per weather condition (fog, cloudy, rainy, sunny) for zero-shot testing. CityScape[7]: Evaluated on 1,525 test images with dynamic vehicle-rich urban scenes, using ground truth from [47].

**HIR Analysis Datasets** ETH3D[40]: We resize this high-resolution ( $6048 \times 4032$ ) dataset to 4K resolution, then randomly cropped to  $1024 \times 320$  per iteration (898 total samples). Virtual KITTI[4] is a synthetic street scene dataset. We processed this dataset identically to real KITTI data.

#### 4.2.2. Performance Comparison

For all the evaluations, only Jasmine\*, E2E FT, and Lotus adopt the least squares alignments. The other self-supervised methods use median alignment. The meanings of each metric are detailed in the supplementary materials.

**KITTI result** To fully demonstrate the advantages of our approach, we compare Jasmine against the most efficient SSMDE models and SoTA SD-based methods. As shown in Table 1, Jasmine achieves the best performance across all metrics on the KITTI benchmark. Notably, our method makes significant progress on the  $a_1$  metric, reflecting an overall improvement in depth estimation accuracy. This systematic advancement stems from the rich prior knowledge of SD. As shown in Fig. 1, without any specialized design for reflective surfaces, our method can accurately distinguish scene elements from their mirror reflections. Additionally, the first row of Fig 5 also demonstrates that our approach preserves structural details better than existing methods. Moreover, when compared to the other SD-based zero-shot models, none of which, including Jasmine\*, use the ground truth depth of KITTI, our method demonstrates a substantial performance advantage, further highlighting the value of self-supervised techniques.

**Generalization Results** Compared to in-domain evaluation, Jasmine exhibits even more remarkable results in zero-shot generalization. Due to the large number of comparison datasets and the unavailability of some models’ open-source code, we only compare with Monodepth2 (the most classic model), MonoViT (renowned for its robustness), MonoViFi (the latest model), and WeatherDepth (trained with additional weather-augmented data, totaling 278k sam-

Table 1. **Quantitative results on the KITTI dataset.** For the **error-based metrics**, the lower value is better; and for the **accuracy-based metrics**, the higher value is better. The best and second-best results are marked in **bold** and underline. Jaeho et al\* is a combined model that applies Jaeho’s[33] (handle dynamic objects) and TriDepth’s[5] (solve edge flatten) approach. Jasmine\* is the same model that uses the least squares alignment. In the data column, Syn, K, and H represent the synthetic, KITTI, and Hypersim datasets, respectively. The number of images and depth labels usage are in brackets. All experiments are conducted at 1024×320 resolution.

Method	Venue	Notes	Data	AbsRel	SqRel	RMSE	RMSElog	$a_1$	$a_2$	$a_3$
E2E FT[32]	WACV2025	ZeroShot	Syn(74K+74K)	0.112	0.649	4.099	0.180	0.890	0.969	0.985
Lotus[21]	ICLR2025	ZeroShot	Syn(59K+59K)	<u>0.110</u>	<u>0.611</u>	<u>3.807</u>	<u>0.175</u>	<u>0.892</u>	<u>0.970</u>	<u>0.986</u>
Jasmine*	-	Mono	KH(68K+0)	<b>0.102</b>	<b>0.540</b>	<b>3.728</b>	<b>0.162</b>	<b>0.907</b>	<b>0.973</b>	<b>0.987</b>
Monodepth2[15]	ICCV2019	Mono	K(40K+0)	0.115	0.882	4.701	0.190	0.879	0.961	0.982
HR-Depth[30]	AAAI2021	Mono	K(40K+0)	0.106	0.755	4.472	0.181	0.892	0.966	0.984
R-MSFM6[60]	ICCV2021	Mono	K(40K+0)	0.108	0.748	4.470	0.185	0.889	0.963	0.982
DevNet[58]	ECCV2022	Mono	K(40K+0)	0.100	0.699	4.412	0.174	0.893	0.966	<u>0.985</u>
DepthSegNet[31]	ECCV2022	Mono	K(40K+0)	0.099	0.624	4.165	0.171	0.902	0.969	<u>0.985</u>
SD-SSMDE[36]	CVPR2022	Mono	K(40K+0)	0.098	0.674	4.187	0.170	0.902	0.968	<u>0.985</u>
MonoViT[56]	3DV 2022	Mono	K(40K+0)	0.096	0.714	4.292	0.172	0.908	0.968	0.984
LiteMono[55]	CVPR2023	Mono	K(40K+0)	0.102	0.746	4.444	0.179	0.896	0.965	0.983
DaCCN[20]	ICCV2023	Mono	K(40K+0)	0.094	0.624	4.145	0.169	0.909	0.970	<u>0.985</u>
Jaeho et al*[5, 33]	CVPR2024	Mono	K(40K+0)	<u>0.091</u>	0.604	<u>4.066</u>	0.164	<u>0.913</u>	0.970	<b>0.986</b>
RPrDepth[19]	ECCV2024	Mono	K(40K+0)	<u>0.091</u>	0.612	4.098	<u>0.162</u>	0.910	<u>0.971</u>	<b>0.986</b>
Mono-ViFI[28]	ECCV2024	Mono	K(40K+0)	0.093	<u>0.589</u>	4.072	0.168	0.909	0.969	<u>0.985</u>
Jasmine	-	Mono	KH(68K+0)	<b>0.090</b>	<b>0.581</b>	<b>3.944</b>	<b>0.161</b>	<b>0.919</b>	<b>0.972</b>	<b>0.986</b>

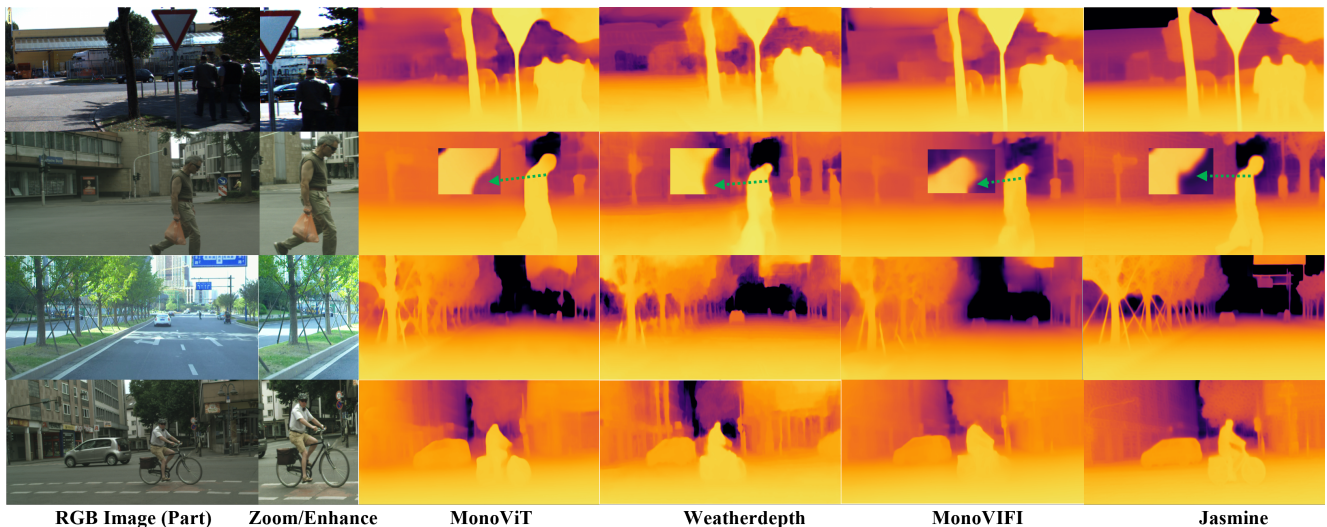


Figure 5. **Qualitative results** on KITTI, DrivingStereo, and CityScape datasets. We compare Jasmine with the most generalizable and best-performing SSMDE methods in both in-domain and zero-shot scenarios.

ples), all of which are self-supervised models. In fact, MonoViT already surpasses the zero-shot capability for nearly all models in the SSMDE, making it a sufficiently strong baseline[26]. Additionally, SD-based methods have excelled in generalization, allowing us to conduct a fair zero-shot comparison here.

As shown in Table 2, Jasmine demonstrated state-of-the-art performance on the datasets of Cityscape and four weather scenarios of driving stereo. Remarkably, our method maintains effectiveness in out-of-distribution (OOD) rainy conditions even without specialized training on weather-enhanced datasets like WeatherKITTI[43]. As illustrated in Fig. 1, Jasmine successfully identifies water surface reflections while producing refined depth estimates. The fine-grain estimation details are further demonstrated

in Fig. 5, pedestrian chins (second row), tree support structures (third row), and bicycle-rider contours (fourth row) are all predicted delicately and precisely. These sharp results were completely disrupted by the reprojection loss in previous self-supervised methods.

### 4.3. Ablation Study

As shown in Table 3, we conduct ablation studies to validate our designs. Firstly, in sub-table (a), we gradually tested the effects of our basic components, such as SD prior, HIR, and SSG. The SD prior proves most critical - training from scratch (ID0 vs. ID1) causes catastrophic failure (AbsRel↑473%, RMSE↑206%). The other experiments also demonstrate that disabling HIR (ID4) or SSG (ID3) degrades performance by 47%/43% in AbsRel, prov-

Table 2. **Quantitative zero-shot results on the CityScape and DrivingStereo dataset.** Alignment protocols and annotation rules follow Table 1’s specifications. The RMSElog and  $a_3$  metrics are omitted for saving space.

Method	AbsRel	SqRel	RMSE	$a_1$	$a_2$
(a)DrivingStereo					
E2E FT[32]	<u>0.160</u>	<u>1.223</u>	<u>5.437</u>	<u>0.795</u>	<u>0.957</u>
Lotus[21]	0.173	1.396	5.816	0.771	0.948
Jasmine*	<b>0.134</b>	<b>0.874</b>	<b>4.666</b>	<b>0.854</b>	<b>0.962</b>
MonoDepth2[15]	0.191	2.865	8.359	0.770	0.923
MonoViT[56]	<u>0.150</u>	<u>1.615</u>	<u>7.657</u>	<u>0.815</u>	<u>0.943</u>
Mono-VIFI[28]	0.158	<u>1.515</u>	<u>6.723</u>	0.798	<u>0.943</u>
WeatherDepth[43]	0.166	1.563	6.986	0.796	0.938
Jasmine	<b>0.136</b>	<b>1.065</b>	<b>5.340</b>	<b>0.850</b>	<b>0.954</b>
(b)Rainy					
E2E FT	<u>0.164</u>	<u>1.438</u>	<u>6.671</u>	<u>0.793</u>	<b>0.963</b>
Lotus[21]	0.167	<b>1.398</b>	6.675	0.775	<u>0.961</u>
Jasmine*	<b>0.159</b>	1.487	<b>6.071</b>	<b>0.825</b>	0.957
MonoDepth2[15]	0.260	4.928	12.577	0.609	0.836
MonoViT[56]	0.190	2.574	9.407	0.724	0.913
Mono-VIFI[28]	0.400	7.480	13.960	0.484	0.726
WeatherDepth[43]	<u>0.166</u>	<u>1.874</u>	<u>8.844</u>	<u>0.748</u>	<u>0.942</u>
Jasmine	<b>0.160</b>	<b>1.684</b>	<b>7.194</b>	<b>0.787</b>	<b>0.950</b>
(c)CityScape					
E2E FT[32]	0.160	1.512	6.944	0.792	0.955
Lotus[21]	<u>0.147</u>	<u>1.344</u>	<u>6.582</u>	<u>0.824</u>	<u>0.965</u>
Jasmine*	<b>0.107</b>	<b>0.770</b>	<b>5.000</b>	<b>0.907</b>	<b>0.982</b>
MonoDepth2[15]	0.158	1.713	8.185	0.783	0.937
MonoViT[56]	0.140	1.416	7.913	0.802	0.944
Mono-VIFI[28]	<u>0.134</u>	1.290	7.372	0.817	0.950
WeatherDepth[43]	0.137	<u>1.130</u>	<b>6.515</b>	<u>0.837</u>	<b>0.968</b>
Jasmine	<b>0.123</b>	<b>1.037</b>	<u>6.618</u>	<b>0.852</b>	<u>0.967</u>
(d)Cloudy					
E2E FT[32]	<u>0.157</u>	<u>1.229</u>	<u>5.522</u>	<u>0.797</u>	<u>0.963</u>
Lotus[21]	0.159	1.263	5.640	0.795	0.959
Jasmine*	<b>0.134</b>	<b>0.910</b>	<b>4.762</b>	<b>0.846</b>	<b>0.968</b>
MonoDepth2[15]	0.192	3.899	10.07	0.775	0.918
MonoViT[56]	<u>0.134</u>	2.028	7.280	<b>0.849</b>	<u>0.955</u>
Mono-VIFI[28]	0.154	<u>1.620</u>	<u>6.883</u>	<u>0.800</u>	0.945
WeatherDepth[43]	0.167	1.956	7.566	0.793	0.934
Jasmine	<b>0.133</b>	<b>1.255</b>	<b>5.651</b>	<b>0.849</b>	<b>0.956</b>
(e)Foggy					
E2E FT[32]	<u>0.141</u>	<u>1.089</u>	<u>6.034</u>	<u>0.836</u>	<u>0.977</u>
Lotus[21]	0.150	1.124	6.173	0.798	0.964
Jasmine*	<b>0.113</b>	<b>0.733</b>	<b>4.883</b>	<b>0.897</b>	<b>0.982</b>
MonoDepth2[15]	0.156	2.556	10.425	0.799	0.921
MonoViT[56]	<u>0.107</u>	1.405	7.899	<u>0.882</u>	<u>0.970</u>
Mono-VIFI[28]	0.160	1.715	8.494	0.769	0.932
WeatherDepth[43]	0.132	<u>1.404</u>	<u>7.679</u>	0.859	0.968
Jasmine	<b>0.098</b>	<b>0.876</b>	<b>5.702</b>	<b>0.902</b>	<b>0.977</b>

ing the necessity of depth distribution alignment and SD detail preservation. In sub-table (b), we further melted down our proposed SSG. ID (6) reveals that the naive GRU-based depth residual refinement, which directly estimates the  $D_\delta$  to update the depth, results in an inferior result. A comprehensive analysis of HIR was conducted in sub-table (c), where IDs (7-10, 0) correspond to Fig. 2 (b-f), respectively. From these experiments, we can draw similar conclusions to Sec. 3.2. The analysis of auxiliary images is presented in sub-table (d). The experiments in IDs (0, 13, 14) indi-

Table 3. **Ablation Studies.** vK and Hy mean the virtual KITTI and Hypersim datasets. Dataset/ $n$  denote we downsample the image to  $\frac{1}{n}$  resolution(*i.e.* Hy/1.6 means downsample to  $640 \times 192$ , where  $640=1024/1.6$ ) and resize them back.

(ID) Method	AbsRel	SqRel	RMSE	$a_1$	$a_2$
Ours					
(0) Jasmine	0.090	0.581	3.944	0.919	0.972
(a) Basic Component					
(1) w/o SD Prior	0.516	6.019	12.06	0.258	0.501
(2) w/o HIR+SSG	0.175	2.264	7.969	0.790	0.929
(3) w/o SSG	0.129	0.938	4.470	0.872	0.956
(4) w/o HIR	0.132	0.673	4.271	0.852	0.967
(b) Scale-Shift GRU					
(5) w/o SSG	0.129	0.938	4.470	0.872	0.956
(6) w/o SST	0.098	0.715	4.350	0.909	0.969
(c) Hybrid Image Reconstruction					
(7) w/o HIR	0.132	0.673	4.271	0.852	0.967
(8) Direct	0.129	0.679	4.385	0.858	0.962
(9) Only Hy	0.106	0.614	4.181	0.901	0.970
(10) Latent space	0.095	0.606	4.138	0.909	0.970
(d) Auxiliary Image Analysis					
(12) KITTI	0.095	0.616	4.040	0.912	0.972
(13) KITTI+ETH3D	0.090	0.586	3.937	0.916	0.972
(14) KITTI+vK	0.094	0.606	4.068	0.911	0.972
(15) KITTI+Hy/4	0.091	0.596	3.943	0.917	0.972
(16) KITTI+Hy/1.6	0.090	0.591	3.971	0.918	0.972

cate that compared to real/synthesis datasets, the content of the dataset is more important, and diverse scenes offer greater benefits than street views similar to our primary dataset, KITTI. Furthermore, IDs (0, 15, 16) demonstrate that our surrogate task is robust to image sampling resolutions, as downsampling to  $\frac{1}{1.6}$  or even  $\frac{1}{4}$  has minimal impact on the results. Moreover, ID(13) further confirms that HIR remains effective even when trained on small-scale datasets (fewer than 1k samples). These insights provide potential opportunities for applying SD models to other dense estimation tasks and enhancing result sharpness.

In summary, these ablation results validate the effectiveness of our proposed adaptation protocol, indicating that each design plays a crucial role in optimizing the diffusion model for self-supervised depth estimation tasks.

## 5. Conclusion

We propose Jasmine, the first SD-based self-supervised framework for monocular depth estimation, effectively leveraging SD’s priors to enhance sharpness and generalization without high-precision supervision. To achieve this object, we introduce two novel modules: Hybrid Image Reconstruction (HIR) for mitigating reprojection artifacts and preserving the Stable Diffusion’s latent priors, alongside Scale-Shift GRU (SSG) to align scale-invariant depth predictions while suppressing noisy gradients. Extensive experiments demonstrate that Jasmine achieves SoTA performance on KITTI and superior zero-shot generalization across datasets. Our approach establishes a new paradigm for unsupervised depth estimation, paving the way for future advancements in self-supervised learning.

# Jasmine: Harnessing Diffusion Prior for Self-Supervised Depth Estimation

## Supplementary Material

### A. Proof of Scale-Invariant Depth

For SSI depth, we assume that the estimated depth  $\hat{D}$  and the ground truth depth  $D$  have the following relationship:

$$\hat{D} = s_c D + s_h$$

Meanwhile, the depth from another viewpoint can be denoted as  $g_1(D')$ . Here,  $g_1$  represents a transformation, and it is straightforward to see that this must be a linear transformation since the known identity only contains linear terms. Introducing a nonlinear transformation would not hold for the depth of arbitrary scenes. Thus, we can define:

$$g_1(D') = a_1 D' + b_1$$

Similarly, we can define the transition as  $g_2(\mathbf{T})$ , which is also a linear transformation, given by:

$$g_2(\mathbf{T}) = a_2 \mathbf{T} + b_2$$

Note that for transformations within the same scene, the relative pose  $\mathbf{R}$  remains constant[18]. Also,  $a$  and  $b$  here can be arbitrary numbers, so we have:

$$g(x) - x \simeq g(x) - a_3 \simeq g(x) \quad (15)$$

Assuming the SSI depth is work, we have:

$$\zeta' g_1(D') = K (\mathbf{R}K^{-1}\zeta(s_c D + s_h) + g_2(\mathbf{T})) \quad (16)$$

Eq. 9 in the paper is:

$$\zeta' s_c D' = K (\mathbf{R}K^{-1}\zeta s_c D + s_c \mathbf{T}) \quad (17)$$

Subtracting Eq. 17 from Eq. 16, we have:

$$\zeta' (g_1(D') - s_c D') = K (\mathbf{R}K^{-1}\zeta s_h + (g_2(\mathbf{T}) - s_c \mathbf{T}))$$

From Eq. 15, it can be simplified as:

$$\zeta' g_1(D') = K (\mathbf{R}K^{-1}\zeta s_h + g_2(\mathbf{T}))$$

Multiplying both sides by  $K^{-1}$ , we get:

$$K^{-1}\zeta' g_1(D') = \mathbf{R}K^{-1}\zeta s_h + g_2(\mathbf{T})$$

This is Eq. 10 in the paper.

### B. Supervision Details

Self-supervised depth estimation has been researched for a decade, and hundreds of works have proposed numerous progressive ideas. Therefore, to achieve SoTA performance,

it is inevitable that we will reuse some loss constraints from previous works to optimize our results. In the following text, except for the **edge loss**, the other losses are mostly referenced from prior papers and are not the core contributions of this paper. Thus, we have not included them in the main paper. The effectiveness of the other papers' losses has been comprehensively proved in their papers, and we did not conduct additional ablation studies for them. For the loss specific in this paper, we present some visualized ablation results in Fig. 6.

**SGD Loss for Dynamic Object.** We first introduce the most commonly used smoothness loss  $L_{sm}$  in self-supervised depth estimation, which encourages locally smooth depth maps while preserving edges in the image. Its specific expression is as follows:

$$L_{sm} = |\partial_x \hat{D}| e^{-|\partial_x \mathbf{I}|} + |\partial_y \hat{D}| e^{-|\partial_y \mathbf{I}|}, \quad (18)$$

where  $\hat{D}$  is the depth normalized by the mean of  $D$ .

Building on this, we adopt the GDS loss (only the first stage) from[33] to handle dynamic objects. This approach is based on the smoothness loss and introduces a ground-contact-prior mask  $M_{gr}$ , defined as:

$$M_{gr}(i, j) = \gamma \cdot M_t(i, j) + (1 - M_t(i, j))$$

where  $M_t$  is the dynamic object segmentation obtained from a semantic segmentation network (1 represents dynamic and 0 for static), and  $\gamma$  is the weighting parameter for  $M_{gr}$ , empirically set to 100. Considering the bottom pixels of dynamic regions like the car tire, they impose a high weighting on  $|\partial_y \hat{d}_t|$  with  $M_{gr}(i, j) = \gamma$ , thereby enforcing its depth consists with its neighboring ground pixels below. So the final loss is:

$$L_{GDS} = |\partial_x \hat{D}| e^{-|\partial_x \mathbf{I}|} + |\partial_y \hat{D}| M_{gr} e^{-|\partial_y \mathbf{I}|}. \quad (19)$$

**Edge Loss for Sharp Prediction.** We further introduce an edge loss to enhance the prediction's details. Since the surrogate and primary tasks are decoupled after the UNet's final layer, and the Scale-Shift Invariant (SSI) depth is shielded from photometric loss interference through SSG-based isolation, the SSI depth retains significantly richer structural details. To transfer these details to the final result, we introduce a simple edge loss. Specifically, we design a GradNet,

$$\text{GradNet}(x) = (|\text{conv2d}(x, w_x)|, |\text{conv2d}(x, w_y)|),$$

Table 4. Additional quantitative results on the KITTI dataset.

Method	Venue	Notes	Data	Resolution	AbsRel	SqRel	RMSE	RMSElog	$a_1$	$a_2$	$a_3$
ManyDepth[47]	CVPR2021	(-1,0)	K(40K+0)	1024×320	0.091	0.694	4.245	0.171	0.911	0.968	0.983
Dual Refine[1]	CVPR2023	(-1,0)	K(40K+0)	960×288	0.087	0.674	4.130	0.167	0.915	0.969	0.984
Mono-ViFI[28]	ECCV2024	(-1,0,1)	K(40K+0)	1024×320	0.089	<b>0.556</b>	<u>3.981</u>	<u>0.164</u>	0.914	0.971	<b>0.986</b>
EPCDepth[35]	ICCV2021	Stereo	K(45K+0)	1024×320	0.091	0.646	4.207	0.176	0.901	0.966	0.983
PlaneDepth[45]	CVPR2023	Stereo	K(45K+0)	1280×384	<b>0.085</b>	<u>0.563</u>	4.023	0.171	0.910	0.968	<u>0.984</u>
Jasmine	-	Mono	KH(68K+0)	1024×320	0.090	0.581	<b>3.944</b>	<b>0.161</b>	<b>0.919</b>	<b>0.972</b>	<b>0.986</b>

where  $w_x = [[-1, 0, 1], [-2, 0, 2], [-1, 0, 1]]$  and  $w_y = [[-1, -2, -1], [0, 0, 0], [1, 2, 1]]$  are the convolutional kernels for computing gradients in the  $x$  and  $y$  directions. Subsequently, the edge loss is defined as:

$$L_e = L_1(C_x, D_x) + L_1(C_y, D_y), \quad (20)$$

where  $(C_x, C_y) = \text{GradNet}(\hat{D}_{\text{SSI}})$  represents the normalized gradient of the detached SSI depth, and  $(D_x, D_y) = \text{GradNet}(\hat{D}_{\text{blur}})$  represents the gradient of blur depth. We implement this edge loss to the SSG outputs  $D_1$  and SI depth  $D_2$ .

The detached  $D_{\text{SSI}}$ , while the depth distribution is inaccurate, has sharper edges, making it an excellent teacher. The prediction comparison with and without edge loss are shown in Fig. 6 (d-4) and (d-3), respectively.

**Sky Loss for Anti-artifact.** Our experiments reveal that (Fig. 6 (b-2)), although the edge loss significantly enhances the model’s details, artifacts still appear outside object edges, particularly in the sky. This is because the sky is a texture-less region, causing self-supervised models to produce erroneous estimates. However, this typically does not affect performance, as during testing, the sky is either cropped (Eigen Crop) or its ground truth depth is invalid and excluded from evaluation. To address this issue, we introduce a sky loss:

$$L_{\text{sky}} = \eta_{\text{sky}} \cdot L_1(D, D_{\text{max}} \cdot \mathbf{1}_D, M_{\text{sky}}), \quad (21)$$

where  $D$  is the predicted depth,  $D_{\text{max}}$  is the maximum depth value,  $\mathbf{1}_D$  is a tensor of ones with the same shape as  $D$ , and  $M_{\text{sky}}$  is the sky mask derived from the semantic segmentation.  $\eta_{\text{sky}}$  is a weighting factor set to 0.1.

Note that the sky loss does not add extra details. As shown in Fig. 6 (b-2) and (b-3), the original details are already captured by the model; the sky loss merely sets the sky depth to infinity.

**Eliminating the Bottleneck of Teacher Loss** In this section, we elaborate on the details of the implementation of teacher loss. We use MonoViT as the teacher model. The model estimates disparity  $dp$ , and thus we obtain the depth  $D_{\text{tc}}$  through:

$$\frac{1}{D_{\text{tc}}} = \text{clip} \left( \frac{1}{D_{\text{max}}} + \left( \frac{1}{D_{\text{min}}} - \frac{1}{D_{\text{max}}} \right) \cdot dp, 0, 3 \right),$$

where  $D_{\text{min}}$  and  $D_{\text{max}}$  are set to 0.1 and 100, respectively. We find that the depth range at range [0,3] can already describe all information within the maximum depth.

For the SSI depth supervision, we perform a normalization similar to Eq. 11 in paper:

$$\text{Norm}(D_{\text{tc}}) = 2 \cdot \left( \frac{D_{\text{tc}} - \min(D_{\text{tc}})}{\max(D_{\text{tc}}) - \min(D_{\text{tc}})} - 0.5 \right). \quad (22)$$

Furthermore, to avoid the performance ceiling imposed by the teacher model, we draw inspiration from D4RD[44], and employ an adaptive filtering mechanism:

$$M_{\text{tc}} = \left[ \min_{t'} ph(\mathbf{I}, \mathbf{I}_{t' \rightarrow t}^{\text{tc}}) < \frac{\lambda}{\eta_{\text{step}}} \right],$$

where  $\lambda$  is a constant set to 1.5,  $\mathbf{I}_{t' \rightarrow t}^{\text{tc}}$  is the warped target image using the teacher disparity  $D_{\text{tc}}$ , and  $\eta_{\text{step}} = \max(1, 30 \cdot (\text{step}_{\text{now}} / \text{step}_{\text{max}}))$  is a dynamic factor that adjusts with training progress. This adaptive weight initially allows the model to converge across the entire depth map and subsequently filters out less accurate regions, mitigating the adverse effects of inaccurate pseudo-depth labels. Therefore, we have:

$$\text{filter}(D_{\text{tc}}) = D_{\text{tc}} \cdot M_{\text{tc}},$$

In the supervision process, we introduce the BerHu loss  $L_B$  and get better results:

$$L_B(x, y) = \begin{cases} |x - y|, & \text{if } |x - y| \leq c, \\ \frac{(x - y)^2 + c^2}{2c}, & \text{if } |x - y| > c, \end{cases} \quad (23)$$

where  $c = 0.2 \cdot \max(|x - y|)$  is a threshold that adapts to the error magnitude. This loss imposes a greater penalty on pixels with larger errors using an  $L_2$ -like penalty, while retaining the robustness of  $L_1$  loss for small errors.

Thus, The Eq. 13 in paper:

$$L_{\text{tc}} = (L_B(\text{norm}(D_{\text{tc}}), D_{\text{SSI}}) + L_B(D_{\text{tc}}, D_1) \cdot \eta_{t1} + L_B(\text{filter}(D_{\text{tc}}), D_{\text{SI}}) \cdot \eta_{t2}) / \eta_{\text{step}}, \quad (24)$$

is fully detailed in this part. The teacher loss not only stabilizes our model but also avoids limiting its performance potential.

**The segmentation model** mentioned above is

Mask2Former[6] throughout. To avoid the misconception that the details stem from the segmentation network’s output, we further expand Fig. 2 (in paper) with segment-based methods. In fact, to preserve these details, a naive approach is to employ semantic segmentation constraints[33]. However, as shown in Fig. 6 (a-2), using the semantic triplet loss from [33] not only disrupts the depth distribution but also introduces spurious edges, rendering it incompatible with SD’s latent priors. Furthermore, the results in paper Table 1 are compared with a segmentation-based model Jaeon et al\*, and our method achieves superior performance.

### C. Evaluation Metrics

Similar to [15], we employ the following evaluation metrics in our experiments,

$$\text{AbsRel: } \frac{1}{|M_{vl}|} \sum_{d \in M_{vl}} |d - d_{gt}| / d_{gt};$$

$$\text{SqRel: } \frac{1}{|M_{vl}|} \sum_{d \in M_{vl}} \|d - d_{gt}\|^2 / d_{gt};$$

$$\text{RMSE: } \sqrt{\frac{1}{|M_{vl}|} \sum_{d \in M_{vl}} \|d - d_{gt}\|^2};$$

$$\text{RMSElog: } \sqrt{\frac{1}{|M_{vl}|} \sum_{d \in M_{vl}} \|\log(d) - \log(d_{gt})\|^2};$$

$a_t$ : percentage of  $d$  such that  $\max(\frac{d}{d_{gt}}, \frac{d_{gt}}{d}) < 1.25^t$ ; where  $d_{gt}$  and  $d$  denote the GT and estimated pixel depth,  $M_{vl}$  is the valid mask set to  $1e - 3 < d_{gt} < 80$ .

### D. Addition Experiments Results

**Regarding SQLdepth** SQLdepth’s authors clarified that they used a new KITTI training split, which included more data than the commonly used split, totaling 70k samples. Later, it was discovered that this training set had a risk of overlapping with the test set, as detailed in the repository’s issues. Consequently, we chose not to compare our work with SQLdepth or its subsequent studies.

**Comparison with Other Self-Supervised Settings** As shown in Table 4, although the multi-frame and stereo-supervision models leverage more information during training and inference, our method still outperforms the state-of-the-art approaches in the corresponding domains across most metrics. This further demonstrates the superiority of our approach.

**Hybrid Ratio Ablation Details** In the paper, fig. 2 (g) illustrates the performance variation versus the hybrid ratio under two supervision schemes. We further present the complete results in Table 5. Note that although “Ph+0” offers better metrics, it predicts blurred results (6 (c-2)).

**Qualitative Comparisons** In Fig. 7, we further compare the performance of our Jasmine with other methods in multi scenes. The quantitative results obviously demonstrate that our method can produce much finer and more accurate

Table 5. **Ablation Studies** on the hybrid ratio. Ph refers to supervision using Eq. 7, while Latent refers to supervision using Eq. 6 (both in paper). The notation  $+\lambda$  denotes the proportion of the KITTI dataset used (e.g., +0.3 indicates a KITTI:Hypersim ratio of 3:7 in the HIR training data.)

(ID) Method	AbsRel	SqRel	RMSE	$a_1$	$a_2$
Ph+0	<b>0.089</b>	<b>0.573</b>	3.973	<u>0.918</u>	<u>0.972</u>
Ph+0.3	<u>0.090</u>	<u>0.581</u>	<u>3.944</u>	<b>0.919</b>	<u>0.972</u>
Ph+0.6	0.092	0.593	<b>3.933</b>	0.915	<b>0.973</b>
Ph+1	0.093	0.590	3.970	0.915	<b>0.973</b>
Latent+0	<u>0.106</u>	<u>0.614</u>	<b>4.181</b>	<u>0.901</u>	<b>0.970</b>
Latent+0.3	<b>0.095</b>	<b>0.606</b>	<u>4.138</u>	<b>0.909</b>	<b>0.970</b>
Latent+0.6	0.121	0.649	4.322	0.876	<b>0.970</b>
Latent+1	0.129	0.679	4.385	0.858	<u>0.962</u>

depth predictions, particularly in complex regions with intricate structures, which sometimes cannot be reflected by the metrics.

### E. Future Work

As noted in paper Sec. 2, the ubiquitously available videos suggest that the self-supervised methods possess significant data advantages and working potential. In this paper, Jasmine is trained on only tens of thousands of data samples, leaving room for further exploration in scaling up training data. We believe that if there really emerges a ‘GPT’ moment for 3D perception in the future, it will more likely involve self-supervised methods trained on the videos rather than learning from annotated depth.

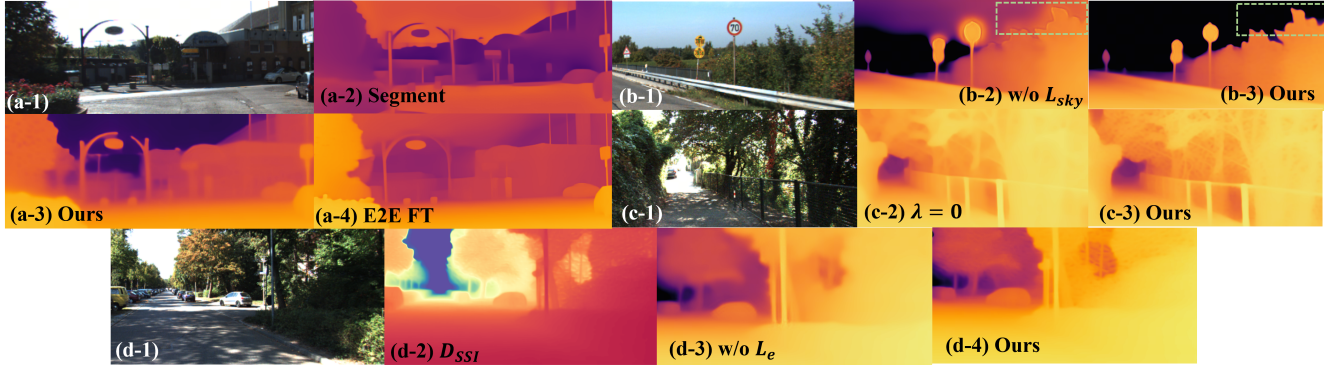


Figure 6. **Qualitative Ablation Study of Adaptive Loss.** Notably, while (a-2) demonstrates superior visual quality, it exhibits an entirely inaccurate depth distribution. (a-4) is the result of E2E FT, which can serve as a pseudo-label here.

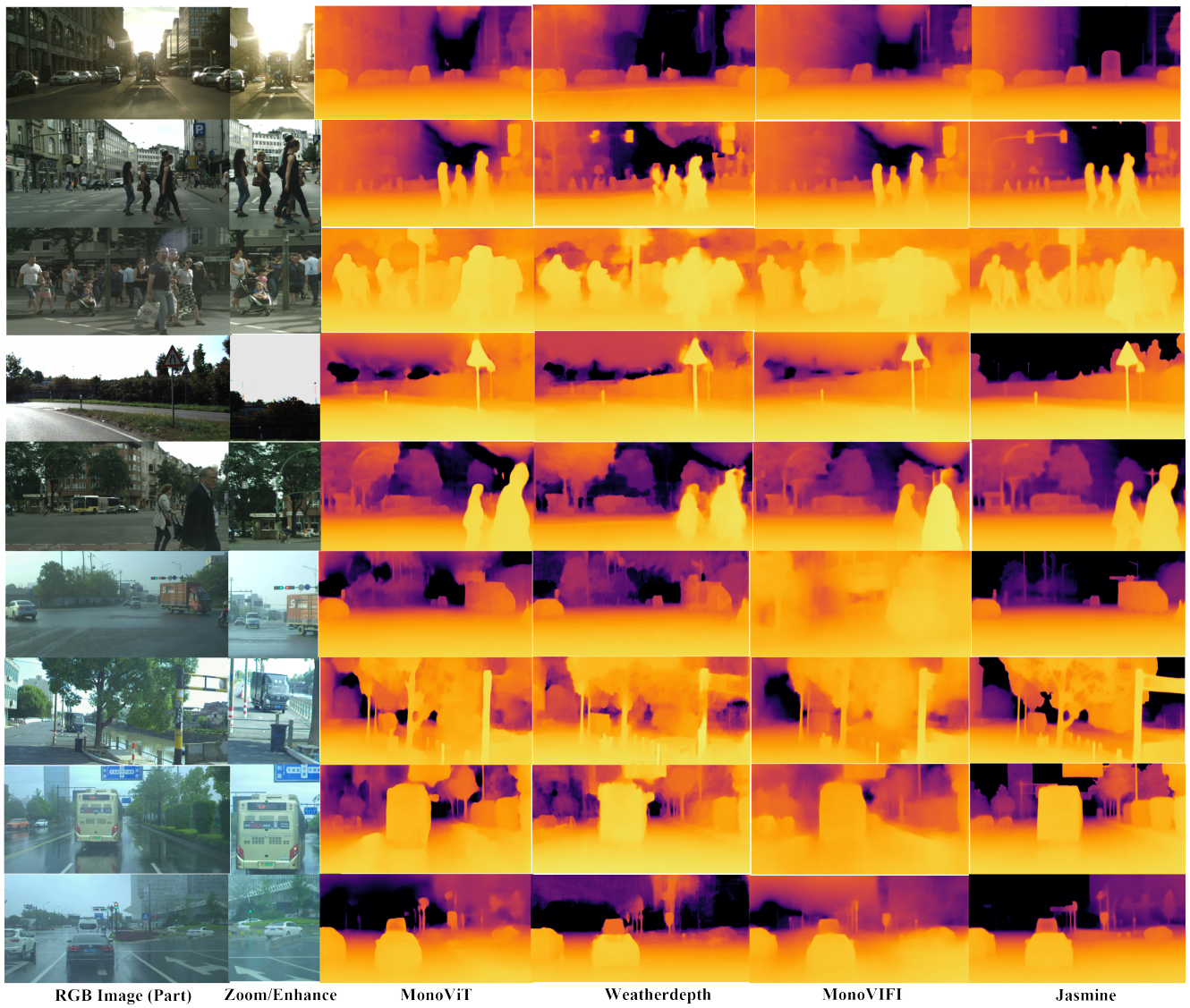


Figure 7. **Qualitative results** on zero-shot Scale-Invariant depth estimation.

## References

- [1] Antyanta Bangunharcana, Ahmed Magd, and Kyung-Soo Kim. Dualrefine: Self-supervised depth and pose estimation through iterative epipolar sampling and refinement toward equilibrium. In *CVPR*, pages 726–738, 2023. 2
- [2] Juan Luis Gonzalez Bello and Munchurl Kim. Forget about the lidar: Self-supervised depth estimators with med probability volumes. In *NeurIPS*, pages 12626–12637, 2020. 2
- [3] Juan Luis Gonzalez Bello and Munchurl Kim. Plade-net: Towards pixel-level accuracy for self-supervised single-view depth estimation with neural positional encoding and distilled matting loss. In *CVPR*, pages 6851–6860, 2021. 2
- [4] Yohann Cabon, Naila Murray, and Martin Humenberger. Virtual kitti 2. *arXiv preprint arXiv:2001.10773*, 2020. 6
- [5] Xingyu Chen, Ruonan Zhang, Ji Jiang, Yan Wang, Ge Li, and Thomas H Li. Self-supervised monocular depth estimation: Solving the edge-fattening problem. In *Proceedings of the IEEE/CVF Winter Conference on Applications of Computer Vision*, pages 5776–5786, 2023. 7
- [6] Bowen Cheng, Ishan Misra, Alexander G. Schwing, Alexander Kirillov, and Rohit Girdhar. Masked-attention mask transformer for universal image segmentation. 2022. 3
- [7] Marius Cordts, Mohamed Omran, Sebastian Ramos, Timo Rehfeld, Markus Enzweiler, Rodrigo Benenson, Uwe Franke, Stefan Roth, and Bernt Schiele. The cityscapes dataset for semantic urban scene understanding. In *CVPR*, pages 3213–3223, 2016. 6
- [8] David Eigen, Christian Puhersch, and Rob Fergus. Depth map prediction from a single image using a multi-scale deep network. *Advances in neural information processing systems*, 27, 2014. 6
- [9] Ziyue Feng, Liang Yang, Longlong Jing, Haiyan Wang, Yingli Tian, and Bing Li. Disentangling object motion and occlusion for unsupervised multi-frame monocular depth. In *ECCV*, pages 228–244, 2022. 2
- [10] Michaël Fonder, Damien Ernst, and Marc Van Droogenbroeck. M4depth: Monocular depth estimation for autonomous vehicles in unseen environments, 2021. 1
- [11] Xiao Fu, Wei Yin, Mu Hu, Kaixuan Wang, Yuexin Ma, Ping Tan, Shaojie Shen, Dahua Lin, and Xiaoxiao Long. Geowizard: Unleashing the diffusion priors for 3d geometry estimation from a single image. *arXiv preprint arXiv:2403.12013*, 2024. 3, 4
- [12] Ravi Garg, Vijay Kumar BG, Gustavo Carneiro, and Ian Reid. Unsupervised cnn for single view depth estimation: Geometry to the rescue, 2016. 2
- [13] Andreas Geiger, Philip Lenz, and Raquel Urtasun. Are we ready for autonomous driving? the kitti vision benchmark suite. In *2012 IEEE conference on computer vision and pattern recognition*, pages 3354–3361. IEEE, 2012. 6
- [14] Clément Godard, Oisín Mac Aodha, and Gabriel J Brostow. Unsupervised monocular depth estimation with left-right consistency. In *Proceedings of the IEEE conference on computer vision and pattern recognition*, pages 270–279, 2017. 2
- [15] Clément Godard, Oisín Mac Aodha, Michael Firman, and Gabriel J Brostow. Digging into self-supervised monocular depth estimation. In *Proceedings of the IEEE/CVF international conference on computer vision*, pages 3828–3838, 2019. 6, 7, 8, 3
- [16] Sylvain Gugger, Lysandre Debut, Thomas Wolf, Philipp Schmid, Zachary Mueller, Sourab Mangrulkar, Marc Sun, and Benjamin Bossan. Accelerate: Training and inference at scale made simple, efficient and adaptable. <https://github.com/huggingface/accelerate>, 2022. 6
- [17] Vitor Guizilini, Rares Ambrus, Dian Chen, Sergey Zakharov, and Adrien Gaidon. Multi-frame self-supervised depth with transformers. In *CVPR*, pages 160–170, 2022. 2
- [18] S. Mahdi H. Miangoleh, Mahesh Reddy, and Yağız Aksoy. Scale-invariant monocular depth estimation via ssi depth. In *Special Interest Group on Computer Graphics and Interactive Techniques Conference Conference Papers '24*, page 1–11. ACM, 2024. 1
- [19] Wencheng Han and Jianbing Shen. High-precision self-supervised monocular depth estimation with rich-resource prior. In *European Conference on Computer Vision*, pages 146–162. Springer, 2024. 2, 7
- [20] Wencheng Han, Junbo Yin, and Jianbing Shen. Self-supervised monocular depth estimation by direction-aware cumulative convolution network. In *ICCV*, 2023. 2, 7
- [21] Jing He, Haodong Li, Wei Yin, Yixun Liang, Leheng Li, Kaiqiang Zhou, Hongbo Zhang, Bingbing Liu, and Yingcong Chen. Lotus: Diffusion-based visual foundation model for high-quality dense prediction. *arXiv preprint arXiv:2409.18124*, 2024. 1, 3, 7, 8
- [22] Jonathan Ho, Ajay Jain, and Pieter Abbeel. Denoising diffusion probabilistic models, 2020. 2
- [23] Yuanfeng Ji, Zhe Chen, Enze Xie, Lanqing Hong, Xihui Liu, Zhaoqiang Liu, Tong Lu, Zhenguo Li, and Ping Luo. Ddp: Diffusion model for dense visual prediction. In *2023 IEEE/CVF International Conference on Computer Vision (ICCV)*. IEEE, 2023. 2
- [24] Bingxin Ke, Anton Obukhov, Shengyu Huang, Nando Metzger, Rodrigo Caye Daudt, and Konrad Schindler. Repurposing diffusion-based image generators for monocular depth estimation. In *Proceedings of the IEEE/CVF Conference on Computer Vision and Pattern Recognition*, pages 9492–9502, 2024. 1, 2, 3
- [25] Neehar Kondapaneni, Markus Marks, Manuel Knott, Rogério Guimarães, and Pietro Perona. Text-image alignment for diffusion-based perception, 2023. 3
- [26] Lingdong Kong, Shaoyuan Xie, Hanjiang Hu, Lai Xing Ng, Benoit R. Cottreau, and Wei Tsang Ooi. Robodepth: Robust out-of-distribution depth estimation under corruptions. In *Advances in Neural Information Processing Systems*, 2023. 7
- [27] Kang Liao, Zongsheng Yue, Zhouxia Wang, and Chen Change Loy. Denoising as adaptation: Noise-space domain adaptation for image restoration. *arXiv preprint arXiv:2406.18516*, 2024. 2
- [28] Jinfeng Liu, Lingtong Kong, Bo Li, Zerong Wang, Hong Gu, and Jinwei Chen. Mono-vifi: A unified learning framework for self-supervised single and multi-frame monocular depth

- estimation. In *European Conference on Computer Vision*, pages 90–107. Springer, 2024. 2, 7, 8
- [29] Ilya Loshchilov and Frank Hutter. Decoupled weight decay regularization, 2019. 6
- [30] Xiaoyang Lyu, Liang Liu, Mengmeng Wang, Xin Kong, Lina Liu, Yong Liu, Xinxin Chen, and Yi Yuan. Hr-depth: High resolution self-supervised monocular depth estimation. In *AAAI*, pages 2294–2301, 2021. 2, 7
- [31] Jingyuan Ma, Xiangyu Lei, Nan Liu, Xian Zhao, and Shiliang Pu. Towards comprehensive representation enhancement in semantics-guided self-supervised monocular depth estimation. In *ECCV*, pages 304–321, 2022. 2, 7
- [32] Gonzalo Martin Garcia, Karim Abou Zeid, Christian Schmidt, Daan de Geus, Alexander Hermans, and Bastian Leibe. Fine-tuning image-conditional diffusion models is easier than you think. In *Proceedings of the IEEE/CVF Winter Conference on Applications of Computer Vision (WACV)*, 2025. 1, 3, 4, 6, 7, 8
- [33] Jaeho Moon, Juan Luis Gonzalez Bello, Byeongjun Kwon, and Munchurl Kim. From-ground-to-objects: Coarse-to-fine self-supervised monocular depth estimation of dynamic objects with ground contact prior. In *Proceedings of the IEEE/CVF Conference on Computer Vision and Pattern Recognition*, pages 10519–10529, 2024. 2, 6, 7, 1, 3
- [34] Adam Paszke et al. Pytorch: An imperative style, high-performance deep learning library. In *NeurIPS*, pages 8026–8037, 2019. 6
- [35] Rui Peng, Ronggang Wang, Yawen Lai, Luyang Tang, and Yangang Cai. Excavating the potential capacity of self-supervised monocular depth estimation. In *ICCV*, pages 15560–15569, 2021. 2
- [36] Andra Petrovai and Sergiu Nedevschi. Exploiting pseudo labels in a self-supervised learning framework for improved monocular depth estimation. In *CVPR*, pages 1568–1578, 2022. 2, 7
- [37] Mike Roberts, Jason Ramapuram, Anurag Ranjan, Atulit Kumar, Miguel Angel Bautista, Nathan Paczan, Russ Webb, and Joshua M Susskind. Hypersim: A photorealistic synthetic dataset for holistic indoor scene understanding. In *Proceedings of the IEEE/CVF international conference on computer vision*, pages 10912–10922, 2021. 6
- [38] Robin Rombach, Andreas Blattmann, Dominik Lorenz, Patrick Esser, and Björn Ommer. High-resolution image synthesis with latent diffusion models. In *Proceedings of the IEEE/CVF conference on computer vision and pattern recognition*, pages 10684–10695, 2022. 2, 6
- [39] Saurabh Saxena, Charles Herrmann, Junhwa Hur, Abhishek Kar, Mohammad Norouzi, Deqing Sun, and David J. Fleet. The surprising effectiveness of diffusion models for optical flow and monocular depth estimation, 2023. 2
- [40] Thomas Schops, Johannes L Schonberger, Silvano Galliani, Torsten Sattler, Konrad Schindler, Marc Pollefeys, and Andreas Geiger. A multi-view stereo benchmark with high-resolution images and multi-camera videos. In *Proceedings of the IEEE conference on computer vision and pattern recognition*, pages 3260–3269, 2017. 6
- [41] Shuwei Shao, Zhongcai Pei, Weihai Chen, Dingchi Sun, Peter C. Y. Chen, and Zhengguo Li. Monodiffusion: Self-supervised monocular depth estimation using diffusion model, 2023. 2
- [42] Jiaming Song, Chenlin Meng, and Stefano Ermon. Denoising diffusion implicit models, 2020. 2
- [43] Jiyuan Wang, Chunyu Lin, Lang Nie, Shujun Huang, Yao Zhao, Xing Pan, and Rui Ai. Weatherdepth: Curriculum contrastive learning for self-supervised depth estimation under adverse weather conditions. In *2024 IEEE International Conference on Robotics and Automation (ICRA)*, pages 4976–4982. IEEE, 2024. 7, 8
- [44] Jiyuan Wang, Chunyu Lin, Lang Nie, Kang Liao, Shuwei Shao, and Yao Zhao. Digging into contrastive learning for robust depth estimation with diffusion models. In *Proceedings of the 32nd ACM International Conference on Multimedia*, pages 4129–4137, 2024. 2
- [45] Ruoyu Wang, Zehao Yu, and Shenghua Gao. Planedepth: Self-supervised depth estimation via orthogonal planes. In *Proceedings of the IEEE/CVF Conference on Computer Vision and Pattern Recognition*, pages 21425–21434, 2023. 2
- [46] Xiaofeng Wang, Zheng Zhu, Guan Huang, Xu Chi, Yun Ye, Ziwei Chen, and Xingang Wang. Crafting monocular cues and velocity guidance for self-supervised multi-frame depth learning. In *AAAI*, pages 2689–2697, 2023. 2
- [47] Jamie Watson, Oisín Mac Aodha, Victor Adrian Prisacariu, Gabriel J. Brostow, and Michael Firman. The temporal opportunist: Self-supervised multi-frame monocular depth. In *CVPR*, pages 1164–1174, 2021. 2, 6
- [48] Haofei Xu, Songyou Peng, Fangjinhua Wang, Hermann Blum, Daniel Barath, Andreas Geiger, and Marc Pollefeys. Depthsplat: Connecting gaussian splatting and depth. *arXiv preprint arXiv:2410.13862*, 2024. 1
- [49] Guorun Yang, Xiao Song, Chaoqin Huang, Zhidong Deng, Jianping Shi, and Bolei Zhou. Drivingstereo: A large-scale dataset for stereo matching in autonomous driving scenarios. In *IEEE Conference on Computer Vision and Pattern Recognition (CVPR)*, 2019. 6
- [50] Lihe Yang, Bingyi Kang, Zilong Huang, Xiaogang Xu, Jiashi Feng, and Hengshuang Zhao. Depth anything: Unleashing the power of large-scale unlabeled data. In *Proceedings of the IEEE/CVF Conference on Computer Vision and Pattern Recognition*, pages 10371–10381, 2024. 2
- [51] Lihe Yang, Bingyi Kang, Zilong Huang, Zhen Zhao, Xiaogang Xu, Jiashi Feng, and Hengshuang Zhao. Depth anything v2. *arXiv preprint arXiv:2406.09414*, 2024. 2
- [52] Zongsheng Yue, Kang Liao, and Chen Change Loy. Arbitrary-steps image super-resolution via diffusion inversion. *arXiv preprint arXiv:2412.09013*, 2024. 2
- [53] Ziyao Zeng, Jingcheng Ni, Daniel Wang, Patrick Rim, Younjoon Chung, Fengyu Yang, Byung-Woo Hong, and Alex Wong. Priordiffusion: Leverage language prior in diffusion models for monocular depth estimation, 2024. 3
- [54] Ning Zhang, Francesco Nex, George Vosselman, and Norman Kerle. Lite-mono: A lightweight cnn and transformer architecture for self-supervised monocular depth estimation. In *CVPR*, pages 18537–18546, 2023. 2
- [55] Ning Zhang, Francesco Nex, George Vosselman, and Norman Kerle. Lite-mono: A lightweight cnn and transformer

architecture for self-supervised monocular depth estimation. In *Proceedings of the IEEE/CVF Conference on Computer Vision and Pattern Recognition*, pages 18537–18546, 2023. [7](#)

- [56] Chaoqiang Zhao, Youmin Zhang, Matteo Poggi, Fabio Tosi, Xianda Guo, Zheng Zhu, Guan Huang, Yang Tang, and Stefano Mattoccia. Monovit: Self-supervised monocular depth estimation with a vision transformer. In *2022 international conference on 3D vision (3DV)*, pages 668–678. IEEE, 2022. [1](#), [2](#), [7](#), [8](#)
- [57] Wenliang Zhao, Yongming Rao, Zuyan Liu, Benlin Liu, Jie Zhou, and Jiwen Lu. Unleashing text-to-image diffusion models for visual perception. *ICCV*, 2023. [3](#)
- [58] Kaichen Zhou, Lanqing Hong, Changhao Chen, Hang Xu, Chaoqiang Ye, Qingyong Hu, and Zhenguo Li. Devnet: Self-supervised monocular depth learning via density volume construction. In *ECCV*, pages 125–142, 2022. [2](#), [7](#)
- [59] Tinghui Zhou, Matthew Brown, Noah Snavely, and David G. Lowe. Unsupervised learning of depth and ego-motion from video, 2017. [6](#)
- [60] Zhongkai Zhou, Xinnan Fan, Pengfei Shi, and Yuanxue Xin. R-msfm: Recurrent multi-scale feature modulation for monocular depth estimating. In *ICCV*, pages 12757–12766, 2021. [2](#), [7](#)